LASER & PHOTONICS REVIEWS
www.lpr-journal.org

Enhancing Transcranial Blood Flow Visualization with Dynamic Light Scattering Technologies: Advances in Quantitative Analysis

Evgeny Zherebtsov, Anton Sdobnov, Oleksii Sieryi, Mika Kaakinen, Lauri Eklund, Teemu Myllylä, Alexander Bykov,* and Igor Meglinski**

A comparative application of major dynamic light scattering (DLS)-based image methodologies applied to transcranial cerebral blood flow imaging is presented. In particular, the study delves into assessing capability of Laser Doppler Flowmetry (LDF), Laser Speckle Contrast Imaging (LSCI), and Diffuse Correlation Spectroscopy (DCS) in enhancing the spatial and temporal resolution of transcranial blood flow imaging. An integral part of the study is focused on the modulation of blood flow through the administration of the vasodilator drug, Sodium Nitroprusside (SNP). This pharmacological intervention facilitated a direct observation of cerebral vasculature's responsiveness to external stimuli, illuminating the physiological adaptations within the brain's microvascular architecture. Advanced LSCI processing techniques are incorporated, notably entropy and principal component analysis (PCA). Entropy is providing a quantifiable measure of the randomness and complexity within the speckle patterns of transcranial blood flow images, revealing remarkably similar outcomes with DSC approach in terms of blood flow dynamics and its quantitative evaluation. The application of PCA approach is provided a more nuanced understanding of blood flow dynamics, facilitating the identification of subtle changes induced by drug administration. This method proved instrumental in enhancing the visualization and detection of nuanced blood flow dynamics, thereby allowing for a more detailed examination of cerebral circulation alterations induced by SNP administration. The study seeks to offer a wider-ranging insight into comprehending the translating further the concept of DLS into transcrainial blood flow vizualization and explore its practical applications, considering hardware, advanced quantitative image processing, and data acquisition.

1. Introduction

Understanding cerebral hemodynamics and blood flow dynamics within the brain is pivotal for unraveling the intricacies of brain function and pathology.[1] In the field of neuroimaging, the visualization and functional assessment of transcranial blood flow have garnered significant attention, fueling the development of advanced imaging techniques.[2,3] Among these, dynamic light scattering (DLS) stands out as a promising approach that offers real-time, non-invasive insights into blood flow dynamics within the cerebral vasculature.[4] DLS harnesses the principles of light scattering and utilizes them to provide valuable information about the movement and velocity of scattering particles.[5] While DLS was originally designed to study Brownian motion,[6] its adaptation to flowing conditions through the use of modified correlation functions analysis makes it a powerful tool for flows monitoring.[7,8] This approach offers the possibility to significantly enhance our comprehension of cerebral blood flow and functional neuroimaging, facilitating important progress in both neuroscience and clinical practices.[4] The spin-off derivative techniques derived from DLS, including Laser Doppler Flowmetry (LDF),[9,10] Diffusing Wave Spectroscopy (DWS),[11,12] and Laser Speckle Contrast Imaging (LSCI),[13,14] are extensively utilized for non-invasive

The ORCID identification number(s) for the author(s) of this article can be found under https://doi.org/10.1002/lpor.202401016

[+]Present address: Department of Human Anatomy and Histology, I.M. Sechenov First Moscow State Medical University, Moscow, Russia

DOI: 10.1002/lpor.202401016

E. Zherebtsov[+], A. Sdobnov, O. Sieryi, A. Bykov
Optoelectronics and Measurement Techniques, Faculty of Information Technology and Electrical Engineering
University of Oulu
Oulu 90014, Finland
E-mail: anton.sdobnov@oulu.fi; alexander.bykov@oulu.fi

imaging of blood flow in the brain, skin, muscles, and other biological tissues.[4] Following advancements in the DWS approach that utilize NIR light for non-invasive measurements, particularly in the direct assessment of local microvascular cerebral blood flow (CBF), these techniques are collectively referred to as Diffuse Correlation Spectroscopy (DCS).[15–18]

In the traditional temporal DCS measurement configuration, a single speckle grain is monitored over time using a highly sensitive single-pixel detector.[19] In speckle ensemble DCS measurements or speckle visibility spectroscopy (SVS),[20] also known as speckle contrast optical spectroscopy (SCOS)[21] or diffuse speckle contrast analysis (DSCA),[22] the method relies on the observation that a rapidly fluctuating speckle pattern captured on a camera with a fixed integration time will exhibit a more uniform appearance compared to a slower fluctuating speckle pattern.[20] The precise determination of speckle decorrelation is achieved by analyzing the overall speckle statistics.

While SVS offers flexibility in temporal fidelity, it grapples with camera noise, particularly as commercial camera sensors tend to be noisier than single-photon counting modules (SPCMs) under low signal light intensity. This challenge becomes pronounced when the signal light produces only a few photoelectron counts per pixel within the exposure time, potentially leading to the signal being overwhelmed by camera noise. One straightforward solution is to extend the camera exposure time, but this introduces a trade-off with a reduction in refresh rate, akin to the trade-off between signal-to-noise ratio (SNR) and measurement time.

A recent proposed technique, interferometric SVS (ISVS),[23] offers a solution to the camera noise predicament. ISVS can effectively capture blood flow dynamics even with a limited number of available signal photons (below 1 photoelectron per pixel). The interference-based detection of ISVS mitigates camera noise by amplifying the weak signal term in the heterodyne cross term. Consequently, the ISVS system achieves a reasonable SNR even when the mean pixel value from the signal light is less than 1. This capability allows ISVS to conduct measurements swiftly within a short acquisition time, generating high-rate CBF estimates in low-light conditions where conventional DCS may fall short.

Since DLS-based techniques do not necessitate the use of contrast agents for visualizing blood flow and offer rapid, non-contact, full-field assessment of microvasculature (particularly in LSCI), they are extensively employed for visualizing tumor vascular network[24] and brain vasculature in both clinical applications[25–27] and animal models.[28–31] Studies have focused on investigating CBF responses to cardiac arrest[32–34] and their correlation with mean arterial pressure.[35] In further studies, the combined use of modern image processing and segmentation approaches, such as Fast Fourier Transform (FFT), Continuous Wavelet Transform (CWT), and Non-negative Matrix Factorization (NMF), reveals blood microflows and their temporal localization in various sensory regions of the brain for several hours postmortem.[36] Continuous monitoring of CBF changes at the individual vessel level has been successfully accomplished in rodents subjected to target temperature management post-cardiac arrest. Further advancements in this approach have enabled monitoring of CBF changes resulting from cerebral ischemia re-perfusion injury.[37] Additionally, various methods have been analyzed for assessing CBF alterations during activation in the somatosensory cortex induced by repetitive whisker stimulation.[38]

Notably, the application of principal component analysis (PCA) has demonstrated a significant reduction in noise within speckle contrast data. Techniques such as fast Fourier transform and general linear model analysis have been employed to estimate cortex activation, contributing to a comprehensive understanding of CBF dynamics during functional activation. A previous study demonstrated that variations in peripheral arterial pressure induced by mesaton injection affect CBF differently in the small and large cerebral blood vessels.

LDF-based systems have been successfully introduced for biomedical applications and pre-clinical studies.[39] Currently, LDF has become a cornerstone technology with widespread applications across various biomedical fields. These applications include the assessment of vascular abnormalities in the brain vasculature,[40] the development of diabetic foot ulcers,[41] the diagnosis of skin vascular complications,[10] and estimation of burn depth,[42] among other critical areas of research.

Chen and colleagues[43] proposed employing standard LSCI in conjunction with microendoscopy to gauge CBF responses amidst hemodynamic shifts at the subcortical tier of the brain. In a similar study, Uchida et al.[44] delved in vivo into scrutinizing acetylcholine release and concomitant blood flow variations within the olfactory bulb in reaction to focused stimulation of the horizontal limb of the diagonal band of Broca. This investigation was facilitated using LSCI and microdialysis. An array of studies[45–47] has presented insights into CBF and brain electrophysiology monitoring pre-, during, and post asphyxial cardiac arrest and subsequent resuscitation, harnessing both LSCI and a fusion of LSCI with electroencephalography. Zhao et al.[48] demonstrated the feasibility of utilizing nanosecond pulse laser sources within LSCI setups for CBF measurements. Liu and team[49] put forth a technique based on short-separation speckle contrast optical spectroscopy, employing point illumination and detection via multi-mode fiber arrays. This methodology was validated during post-stroke brain vasculature observation in an animal model, exhibiting enhancements in signals from static and slow tissue components when compared to standard LSCI. An innovative multi-modal approach combining LSCI, fluorescence spectroscopy, and diffuse reflectance spectroscopy, as reported by Piavchenko et al.[34], effectively discriminates

M. Kaakinen
Biocenter Oulu
University of Oulu
Oulu 90014, Finland
L. Eklund
ECM and Hypoxia, Faculty of Biochemistry and Molecular Medicine
University of Oulu
Oulu 90014, Finland
T. Myllylä
Health Sciences and Technology, Faculty of Medicine
University of Oulu
Oulu 90014, Finland
I. Meglinski
College of Engineering and Physical Sciences
Aston University
Aston St, Birmingham B4 7ET, UK
E-mail: i.meglinski@aston.ac.uk

hemodynamic variations within the mouse brain vasculature following cardiac and respiratory arrest.

Comparative studies of LSCI and LDF have demonstrated that while both techniques are effective in assessing cutaneous microvascular function, LSCI generally offers superior reproducibility and reliability, particularly in measuring blood flow changes in shallow skin layers.[50] It has also been shown that while both methods are useful, their data are not interchangeable due to inherent biases and differences in the measurements.[51,52] Indeed, although these methods may seem identical, they differ in the technical requirements imposed on measuring intensity fluctuations and the spectral power of scattered light, which are related to each other via the Wiener–Khinchin theorem.[4] In addition, when comparing LDF and LSCI, the basic implementation of LDF allows for flow assessment at only a single point in the observed medium. To assess blood flow over larger areas, a scanning mode must be implemented in the LDF setup. However, using the scanning mode results in increased measurement time compared to full-field single-shot imaging. However, scanning mode results in increased measurement time comparing to full-field single shot imaging. Serov et al.[53–55] introduced optical setup combining standard LDF and high-speed CMOS camera allowing for full-field Doppler-shifted light measurement and comparing of LSCI and LDF measurements.

Several studies have explored the limits of DLS and LSCI in non-ergodic conditions.[56–59] Experiments using Intralipid solution phantoms with varying static layer thicknesses show that a thick layer of static scatterers above the dynamic layer does not significantly affect speckle contrast processing.[60] This finding is validated through transcranial visualization of mouse brain vasculature, considering typical mouse skull thickness.[61,62] The studies emphasize the importance of proper selection of LSCI/DLS imaging parameters, including exposure time and frame quantity, to mitigate non-ergodic effects in measurements. It also provides a rationale for identifying limitations of DLS-based imaging in accurately quantifying transcranial blood flow under disrupted ergodicity conditions.

In this paper, we conduct a comparative analysis of the primary DLS-based imaging modalities,[4] such as LDF, LSCI, and DCS with a focus on their efficiency and optimal applicability for transcranial visualization of blood flow and in vivo functional imaging of brain hemodynamics. Furthermore, the conventional DLS-based modalities discussed above, our assessment includes entropy-based laser speckles processing[63] and principal component analysis (PCA)[64] applied to the resulting blood flow images. Harnessing the potential of augmented insights into transcranial blood flow imaging, coupled with advancements in the light scattering paradigm, signal processing, and multidetector configurations, our objective is to present an improved methodology. This methodology is designed to tackle the challenges arising from the intricate nature of brain tissue and the demand for time-resolved imaging. Through the incorporation of NIR wavelengths and the integration of time-correlated photon counting, our aim is to amplify penetration through the skull and brain tissue, simultaneously enhancing the precision and resolution of blood flow measurements.

Leveraging the capabilities of enhanced insights into transcranial blood flow imaging in conjunction with advancements in light scattering paradigm, signal processing, and multidetector configurations, we seek to propose a refined methodology that addresses the challenges posed by the complex nature of brain tissue and the need for depth-resolved imaging. By utilizing near-infrared wavelengths and integrating time-correlated photon counting, we aim to enhance penetration through the skull and brain tissue while improving the accuracy and resolution of blood flow velocity measurements.

2. Dynamic Light Scattering Technologies for Transcranial Blood Flow Imaging

Within the framework of DLS-based methodologies employed for blood flow imaging, the principal metric of interest is derived from the temporal variations in light intensity scattered within biological tissues.[4] These perturbations are primarily attributable to the motion of particulate scatterers, notably erythrocytes. Quantitatively, the temporal fluctuations in intensity are encapsulated by the auto-correlation function of intensity, expressed as:

$$g_2(\tau) = \frac{\langle I(t)I(t+\tau)\rangle}{\langle I(t)^2\rangle} \tag{1}$$

where $I(t)$ and $I(t+\tau)$ represent the intensities of scattered light at temporal instants t and $t+\tau$, respectively. Moreover, a deeper insight into these fluctuations necessitates an understanding of their relation to the electric field through the lens of optical coherence. The temporal auto-correlation function of the electric field, which delineates the coherence characteristics of the electric field of scattered light, is defined as:

$$g_1(\tau) = \frac{\langle E(t)E^*(t+\tau)\rangle}{\langle E(t)E^*(t)\rangle} \tag{2}$$

with $E(t)$ denoting the electric field of the detected light. Intriguingly, there exists a relation between these two functions, $g_1(\tau)$ and $g_2(\tau)$, known as the Siegert's relation:

$$g_2(\tau) = 1 + \beta|g_1(\tau)|^2 \tag{3}$$

where β embodies the specifics of the optical configuration of the experimental setup. This parameter is not inherently associated with the dynamics of the scattering entities but is rather tied to attributes such as the polarization and coherence of light, and certain instrumental parameters. The significance of the Siegert's relation is manifold; not only does it permit the extraction of $g_1(\tau)$ from the empirically measured $g_2(\tau)$, but it also serves as a critical bridge, especially when considered in conjunction with the Wiener–Khintchine theorem, thereby establishing an intricate linkage between the spectral breadth of the light and the correlation duration of its intensity perturbations.

2.1. Laser Doppler Flowmetry

An algorithm akin to the one employed in LDF was utilized for blood perfusion calculation, based on the Fourier transform of the autocorrelation function. The signal processing procedure

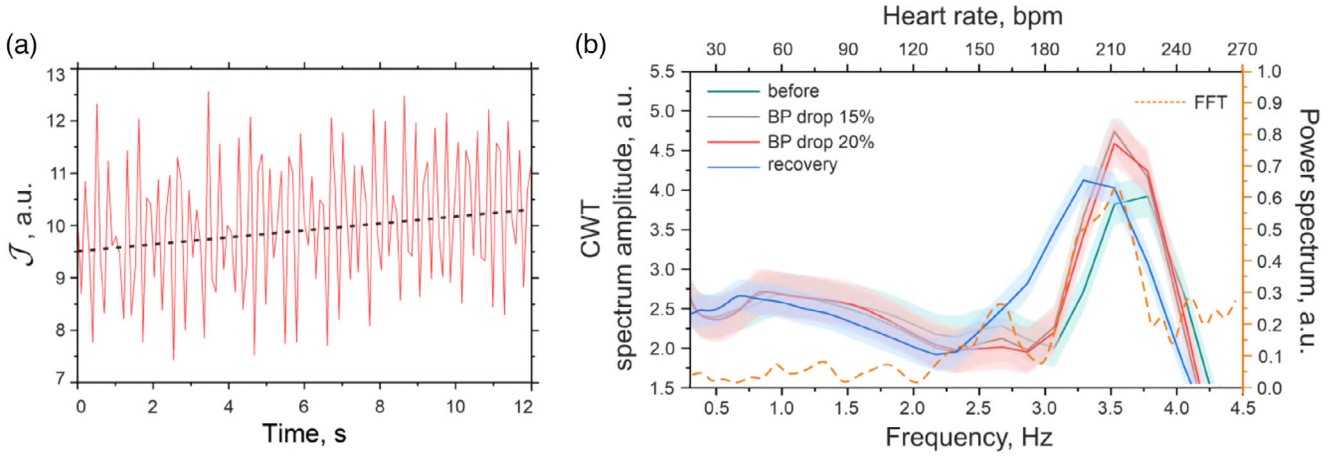

Figure 1. a) A representative trace of blood flow time-series recorded transcranially in a cortex blood vessel and b) CWT spectra for the experiment with sodium nitroprusside infusion. Here, green color corresponds to data before infusion, gray color - to 15% blood pressure drop after infusion, red color - to 20% blood pressure drop after infusion, and blue color - to recovery after infusion. Dashed line (orange) corresponds to power spectrum of $\mathcal{J}$ shown at (a) and calculated via fast Fourier transform.

central to the visualization of blood perfusion in LDF adhered to a well-established expression[65]:

$$\mathcal{J} = \frac{\int_{\omega_1}^{\omega_2} \omega \cdot S[g_2(\tau) - 1]d\omega}{\langle I \rangle} \tag{4}$$

where $\mathcal{J}$ is the blood perfusion index measured in arbitrary units (a.u.); $S[g_2(\tau) - 1]$ is the power spectrum of the resulting recording retrieved from the intensity fluctuation in a pixel of the camera sensor; $\langle I \rangle$ is the average DC signal from the pixel.

2.1.1. Spectral Analysis of Time-Series Blood Flow

In the study, we visualized the parameters characterizing cortex microcirculation oscillations, in conjunction with the autocorrelation features inherent to the perfusion time series. In a recent study, a similar approach based on the LSCI was employed to visualize respiratory and cardiac oscillations.[66] To decipher the intricacies of the microcirculatory blood flow regulatory mechanisms, we employed continuous wavelet analysis (CWT) on the calculated full-field blood perfusion time series, denoted as $\mathcal{J}(t)$. The spectral assessment of these signals was facilitated using MATLAB, adopting the complex-valued Morlet wavelet for this analytical expression.

The wavelet transform of a blood perfusion time-series $\mathcal{J}(t)$, represented as $W_x(f_{osc}, \tau)$, was articulated concerning the designated mother wavelet $\psi(t)$, as explicated in Equation (5):

$$W_x(f_{osc}, \tau) = \sqrt{f_{osc}} \int_{\infty}^{\infty} \mathcal{J}(t)\psi^*[f_{osc}(t - \tau)]dt \tag{5}$$

Here, t represents time, τ represents the temporal shift of the wavelet, f_{osc} serves as an approximation of the oscillation frequency (represented as $\sim 1/a$, wherein a delineates the wavelet's time-scale), and the symbol * demarcates the complex conjugation operation. The Morlet wavelet can be explicitly characterized as:

$$\psi(t) = e^{2\pi i t} e^{-t^2/2\sigma^2} \tag{6}$$

Employing the aforementioned function empowers us to discern the amplitude and phase attributes of oscillations across varying frequencies within the signal under scrutiny. Furthermore, the integrated wavelet spectrum was computed through the integration of Equation (5) across a temporal span T of the time-series recordings, articulated as:

$$M_{osc}(f_{osc}) = \frac{1}{T} \int_0^T |W_x(f_{osc}, \tau)|^2 d\tau \tag{7}$$

Wavelet analysis of the LDF signal unveiled the presence of five distinct oscillatory components. These components span various frequency bands, each resonating with unique physiological mechanisms steering blood flow regulation. **Figure** 1a shows an example of typical oscillations in the blood flow in the sagittal sinus of a mouse recorded transcranially and calculated for one pixel using parameter $\mathcal{J}$.

The introduction of sodium nitroprusside modulated arterial blood pressure (BP), leading to changes in relative blood pulsations in the visualized vessels. Figure 1b displays the averaged spectrum of oscillations in the range of the mouse's heart rate frequencies for four stages of experiment: the first stage is pre-infusion; the second stage is during sodium nitroprusside infusion when the average pressure dropped by 15%; the third stage us during infusion when the average pressure decreased by 20%; and fourth stage is recovery after stopping the drug infusion. Also, this figure displays the power spectrum of $\mathcal{J}$ shown in Figure 1a and calculated via fast Fourier transform. It can be seen that for all four stages of experiment the heart rate frequency takes values ≈ 3.5 Hz (or 210 ± 15 beats per minute).

Further, we calculated relative changes in the amplitude of pulsations at 3.5 Hz frequency. **Figure** 2a–c shows the relative change in the amplitude of pulsations corresponding to

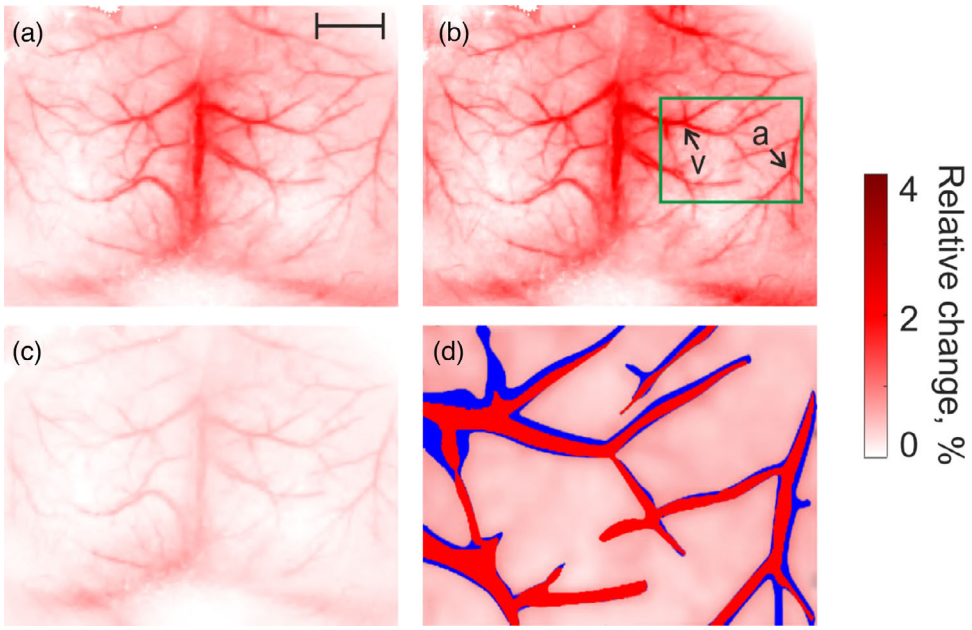

Figure 2. Visualization of the relative changes in the amplitude of pulsations corresponding to 15% blood pressure drop (a), 20% blood pressure drop (b) and recovery (c) in comparison to the level before the start of sodium nitroprusside infusion. d) Visualization of threshold masks applied to vessel structure after recovery (red color) and at 20% blood pressure drop (blue color) in area of interest (green rectangle at (b) where a corresponds to artery and v corresponds to vein). Scale bar is equal 2 mm.

15% blood pressure drop, 20% blood pressure drop and recovery in comparison to the level before the start of infusion. The figures indicate that sodium nitroprusside infusion resulted in up to a 3% change in amplitude pulsation within the brain vasculature at a heart rate of 3.5 *Hz*. Notably, following the recovery period, the amplitude pulsation nearly returned to the baseline control values. Additionally, we applied threshold masks to the vessel structures both before the infusion and at a 20% reduction in blood pressure. As shown in Figure 2d, the vessel diameter increased following the sodium infusion. A rough estimation suggests a 10 – 20% increase in diameter during vasodilation, which is consistent with previous findings.[67]

Thus, frequency analysis using wavelet transformation allows for functional imaging to identify areas of greatest drug impact on blood flow, including stages of vasodilation and vasoconstriction.

2.1.2. Principle Component Analysis

In recent years, the application of Principle Component Analysis (PCA) to image analysis has gained significant attention within the image processing community.[64,68] PCA, a statistical method used for dimensionality reduction and highlighting variation in datasets, has proven effective across various imaging modalities, notably enhancing transcranial blood flow reconstruction in small laboratory animals and addressing key challenges in this domain.

One of the primary challenges in transcranial imaging is the presence of noise from sources such as equipment anomalies, ambient conditions, and involuntary subject movement. PCA effectively mitigates this by focusing on the principal components that capture the most variance, enhancing the visibility of critical features and improving the identification of regions with altered blood flow dynamics. Additionally, the substantial datasets produced by transcranial imaging necessitate efficient data management. PCA addresses this by compressing data through dimensionality reduction, which minimizes information loss, conserves storage space, and accelerates computational processing, crucial for high-resolution images.

PCA when applied to the image analysis, is represented by data matrix Φ, where each row corresponds to a different pixel or region, and each column represents the intensity at a different time point Φ.[69] The core of PCA involves computing the covariance matrix from this data matrix, which captures how the intensity values across different time points or spatial regions co-vary. This covariance matrix is crucial because it encapsulates the underlying correlations within the speckle patterns, reflecting both dynamic and static components of the tissue being imaged.

In the analysis of LDF imaging data, PCA is used to extract and differentiate between various signal components, including the true physiological signals and noise. The first three principal components (PCs) are often retained because they capture the most significant variance in the data.

Figure 3a–i presents a representative example of PCA decomposition of the transcranially measured perfusion signal, based on an algorithm utilizing spectral power density analysis of signal fluctuation in a pixel (LDF blood perfusion visualization). The introduction of SNP led to a decrease in the animal's mean arterial pressure. In this context, the PCA components PC1, PC2, and PC3 convey distinct information about the redistribution of blood flow. In Figure 3 PC1 correspond to the general displacement of RBC or blood flow within the tissue across the entire imaged area, PC2 highlights regional changes in blood flow that differ from

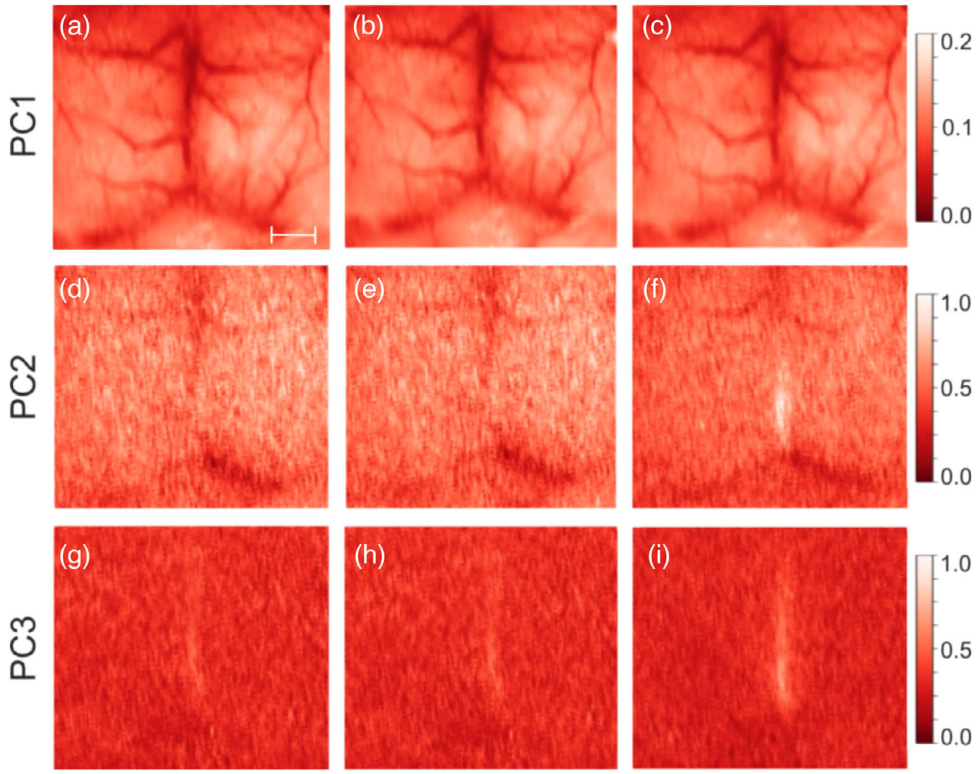

Figure 3. Visualization of PCA components before (a,d,g) and during infusion of SNP (b,c,e,f,h,i) when the mean BP dropped by 15% and 20%, respectively. Scale bar is equal 2 mm.

the global pattern captured by PC1, and PC3 captures small-scale or less coherent movements within the tissue that contribute to the overall variance. Notably, the PC2 component demonstrates significant changes in blood flow in the animal's sagittal sinus when the pressure drops by 20%.

The mathematical link between $\mathcal{J}$ and PCA (and/or $g_2(\tau)$ and PCA, see (4) is indirect, where the correlation function $g_2(\tau)$ influences the covariance structure of the data, and PCA then extracts the major axes of variance from this covariance structure. The PCs can be thought of as capturing the dominant patterns of correlation present in the data Φ, but they do so by analyzing the covariance matrix rather than directly measuring the correlation functions.

2.2. Laser Speckle Contrast Imaging

Temporal speckle contrast, often used in LSCI to assess blood flow dynamics, can be derived from the autocorrelation function.[69] The second-order intensity autocorrelation function, denoted as $g_2(\tau)$, relates to the field autocorrelation function $g_1(\tau)$ via the Siegert's relation (3). The temporal speckle contrast K is typically defined as the ratio of the standard deviation σ to the mean speckle intensity $\langle I \rangle$, i.e.:

$$K = \frac{\sigma}{\langle I \rangle} \tag{8}$$

In the context of DLS and LSCI, K can be linked to the decay time τ_c of $g_2(\tau)$.[70] The speckle contrast $K(T)$, influenced by the digital camera exposure time T, is expressed in terms of the autocorrelation function as:

$$K(T) = \sqrt{\frac{2\beta}{T}\int_0^T \left|\frac{g_1(\tau)}{g_1(0)}\right|^2 \left(1 - \frac{\tau}{T}\right) d\tau} \tag{9}$$

where $K(T)$ is the speckle contrast as the function of the digital camera exposure time T. The parameter $1/K^2$ is a more convenient way of obtaining blood perfusion measurements with the speckle contrast technique since the parameter increases with the increase of the blood flow.[43,71,72]

Figure 4a illustrates a representative example of transcranial imaging of brain vessels utilizing temporal speckle contrast. The clarity of this vascular bed image facilitates the confident identification of all principal vascular components.

2.3. Diffuse Correlation Imaging

The video camera's frame rate is not always sufficient to fully reconstruct the autocorrelation function for subsequent determination of blood flow parameters. In the case of transcranial imaging of mouse brain vessels, the required frame rate may reach several thousands of frames per second. This also necessitates the use of a high-power single-mode laser (over 50 $mWcm^{-}2$), complicating its selection and causing excessive tissue heating. The parameters of the camera used in this study allow for the recording of the autocorrelation intensity value at a temporal delay of $10^{-4}s$ with a resolution of 100×150 pixels. For the mentioned imag-

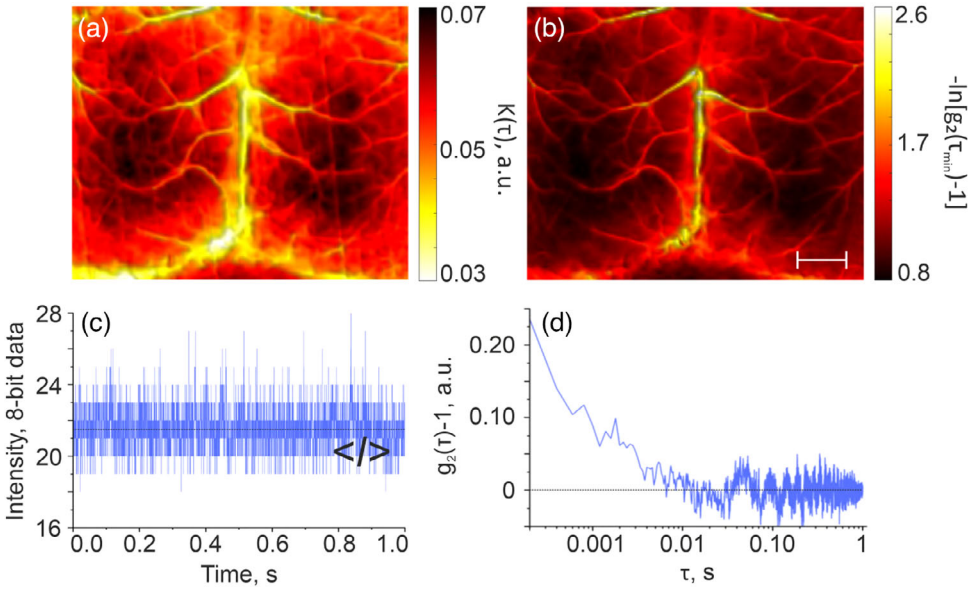

Figure 4. Representative examples of transcranial imaging using LSCI (a) and the autocorrelation function value in the area of its steepest slope (b). A representative trace of the intensity fluctuations of the back-scattered light observed in a single pixel of the camera (c) and the corresponding calculated ACF (d). Scale bar is equal 2 mm.

ing parameters, an example of the recorded intensity fluctuation at an individual pixel, along with the corresponding calculated autocorrelation function curve, is presented in Figure 4c, respectively. From Figure 4d, it is evident that only the rising section of the autocorrelation can be reconstructed, but it is not possible to record it in its entirety. In this case, the classical method of reconstructing blood flow through fitting an analytical function becomes problematic or impossible.

An alternative to fitting could be the use of the autocorrelation function value in the area of its steepest slope as a metric for blood flow visualization. With an increase in the speed and volume of flowing blood, the leftward shift of the autocorrelation function leads to a decrease in the autocorrelation values at the point. A decrease in blood flow leads to an increase in autocorrelation for the same temporal shift value. The experiment demonstrates that the metric $\ln[g_2(\tau_{\min}) - 1]$ provides a better linear characteristic than the parameter of autocorrelation function without logarithmic transformation.

Figure 4b shows a typical example of transcranial imaging using this metric. This approach enables clear visualization of the sagittal sinus, individual terminal veins, and arterioles, allowing for one high-quality image per second with significantly reduced noise compared to temporal speckle contrast imaging with the same frame accumulation time.

Another alternative characteristic is the maximum slope of the autocorrelation function constructed in a logarithmic scale $\max[\nabla g_1(\tau^{1/2})]$. The parameter we used in our analysis was calculated from the autocorrelation function available for the camera frame rate. A representative example of transcranial imaging of vessels with the parameter $\max[\nabla g_1(\tau^{1/2})]$ is presented in **Figure** 5c. The resulting image clearly visualizes the sagittal sinus, as well as major arteries and veins.

2.4. Entropy-Based Imaging

Traditional entropy-based algorithms are used to measure the regularity or orderliness of a time series of physiologic signals in health and disease.[73] Entropy tends to increase with the level of disorder, reaching its maximum for entirely random systems. However, it is important to note that an increase in entropy does not always correspond to a rise in dynamical complexity. For instance, a randomized time series exhibits higher entropy compared to the original time series. Nevertheless, the generation of surrogate data in this process breaks down correlations and diminishes the information content of the initial signal.

In the context of assessing blood flow using light backscattered from biological tissue, this method involves utilizing two sets of experimentally measured intensity fluctuations obtained from neighboring pixels in the resulting laser speckle images.[63] The first set comprises intensity fluctuations, each spanning m consecutive time points, while the second set follows the same pattern but with $m + 1$ time points. Within each set, pairs of intensity fluctuations are subjected to comparison. A threshold value "r" is employed to determine similarity. If the element-wise difference between two intensity fluctuations exceeds the "r" threshold, a similarity value of zero is assigned. Conversely, if the difference falls below "r," a similarity value of one is assigned.

To quantify the similarities between the two sets, the negative natural logarithm is calculated of the conditional probability that similarities observed in the first set of intensity fluctuations endure in the second set. This process yields an entropy measure that characterizes the temporal and spatial complexity of the laser speckle pattern. Consequently, this method offers insights into the underlying properties of the tissue and the dynamics of blood flow in vivo. The obtained entropy quantifies similarities and merely tallies the occurrences of these similarities.

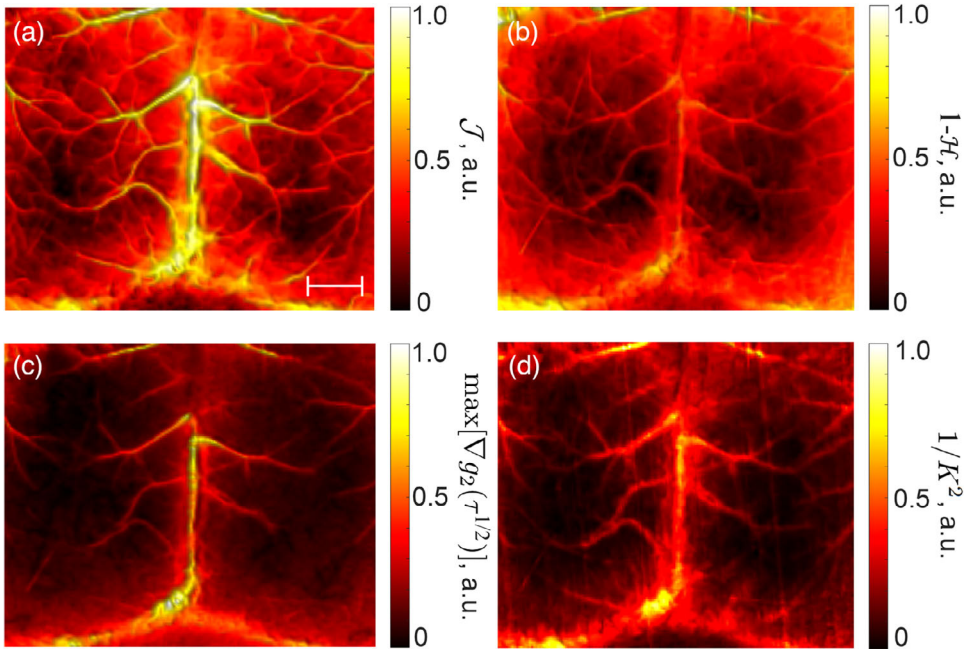

Figure 5. Representative images of transcranial blood perfusion vad flow speed mapping in the murine model with the LDF-based parameter $\mathcal{J}$ (a); the entropy $\mathcal{H}$ (b); the maximum slope of the autocorrelation function constructed in a logarithmic scale max$[\nabla g_1(\tau^{1/2})]$ (c); and Imaging with the LSCI based $1/K^2$ parameter (d). Scale bar is equal 2 mm.

Given a discrete speckle image, let us represent the intensity of the i^{th} pixel as I_i, where $i \in \{1, 2, \ldots, N\}$ and N is the total number of pixels.

To compute the entropy, the balanced estimator of Shannon entropy is used:[74]

$$\mathcal{H} = \frac{1}{N+2} \sum_{i=1}^{M} \left[(n_i + 1) \sum_{i=n_i+2}^{N+2} \frac{1}{j} \right] \tag{10}$$

where N is the size of data set, M is the maximum gray level value for captured frames, and n_i is the value of the ith gray level.

The computed entropy value $\mathcal{H}$ from Equation (10) is used to visualize blood flow (see Figure 5b). The resulting entropy map is visualized similarly to a traditional LSCI image (see Figure 5), where regions of higher entropy indicates higher blood flow and vice versa. For a region of the image (or for individual pixels), a lower entropy value indicates a more dynamic scatterer presence (e.g., moving RBC) and hence higher blood flow, whereas a higher entropy indicates lesser or static flow. Further, to make it in the opposite way, we operate with $1 - \mathcal{H}$ value.

Thus, entropy-based imaging provides an alternative approach to traditional LSCI. While there is no simple direct formula connecting the correlation function and entropy in general cases, they are conceptually linked. The correlation function influences the distribution of intensity values in the speckle pattern, which in turn affects the entropy. In specific models, such as Gaussian processes, there can be an approximate logarithmic relationship between entropy and correlation time[63]:

$$\mathcal{H} \sim \frac{1}{2} log(\tau_c) \tag{11}$$

where

$$\tau_c \approx \int_0^\infty g_2(\tau) d\tau \tag{12}$$

By focusing on the variability and unpredictability in the speckle pattern, entrope offers unique insights and a potentially more robust metric for blood flow visualization. An example of the image obtained transcranially using the visualization of parameter $\mathcal{H}$ is shown in Figure 5b. The contrast of the obtained image is inferior to images acquired using calculations based on power spectrum analysis and speckle contrast computation (see Figures 5a and 4a). Nonetheless, it should be noted that the quality of this image does not match that achieved by methods that analyze the autocorrelation function or employ the LDF technique. Figure 5d displays another example of imaging, this time employing the $1/K^2$ parameter.

One should consider, that while the correlation function $g_2(\tau)$ in LSCI typically refers to the temporal changes in the speckle intensity patterns, it describes how the speckle intensity at a given point varies over time, which is related to the motion of the scattering particles (i.e., RBC). Faster motion leads to quicker decorrelation of the speckle pattern, resulting in a shorter correlation time. Entropy, in the context of LSCI, refers to the degree of randomness or disorder in the speckle pattern. Higher entropy corresponds to a more random and disordered speckle pattern, which typically occurs when the underlying dynamic process is more complex or involves multiple scattering events with different time scales. Lower entropy indicates a more ordered speckle pattern, suggesting less complex dynamics or more uniform motion of scatterers.

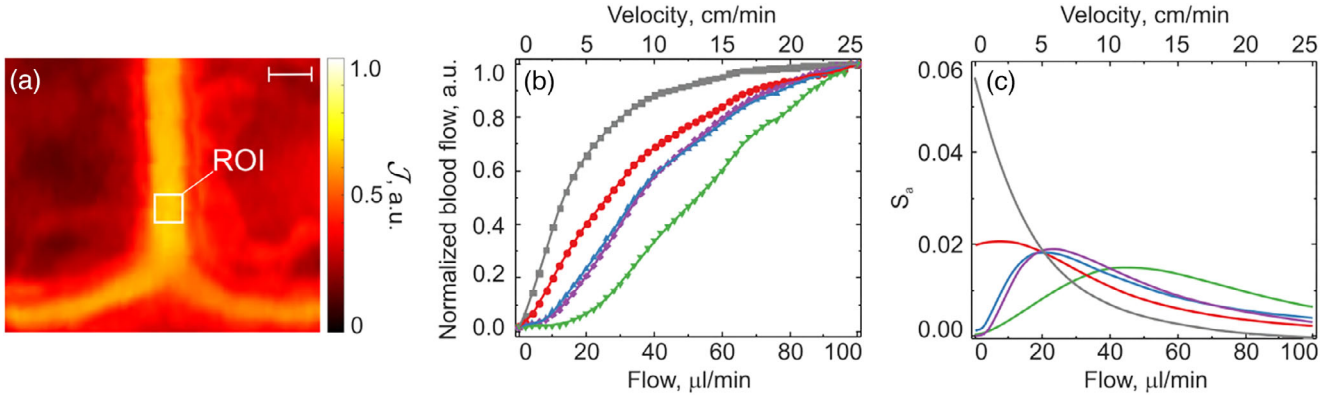

Figure 6. a) The area of blood flow quantitative measurements in the phantom of small animal brain. Scale bar is equal 2 *mm*; b) Comparison of the change of the normalized flow estimated by different DLS-based methods with the change of flow in the phantom: gray line $\mathcal{J}$ – the blood perfusion index by LDF; red line $\ln[g_2(\tau_{min})-1]/\Delta\tau$ – the steepest slope of the temporal intensity autocorrelation function in the area; blue line $max[\nabla g_1(\tau^{1/2})] \equiv grad(g_1(\tau^{1/2}))$ – the maximum slope of the temporal field autocorrelation function; purple line $1-H$ – the entropy; green line $1/K^2$ – the inverse square spatial speckle variance ($K(T)$) proportional to the speed of moving particles (more details in the text); c) Sensitivities corresponding to each DLS-based approach presented in Figure 6b.

In addition, while the correlation function in LSCI typically refers to the temporal of the speckle intensity patterns, and describes how the speckle intensity at a given point changes over time, that is related to the motion of RBC: faster motion leads to quicker decorrelation of the speckle pattern, and thus, a shorter correlation time. Entropy in the context of LSCI refers to the degree of randomness or disorder in the speckle pattern. Higher entropy corresponds to a more random and disordered speckle pattern, which typically arises when the underlying dynamic process is more complex or involves multiple scattering events with different time scales. Lower entropy indicates a more ordered speckle pattern, suggesting less complex dynamics or more uniform motion of scatterers.

2.5. Cross-Validation of DLS-Based Approaches for Blood Flow Evaluation

Figure 6 presents a quantitative comparison of the results derived from direct measurements of absolute flow rate in the phantom of small animal brain.[75,76] These measurements were independently obtained using the perfusion index by LDF denoted as $\mathcal{J}$, the autocorrelation function value of DCS in the region of its steepest slope represented as $\ln[g_2(\tau_{min})-1]$, and the maximum slope denoted as $\max[\nabla g_1(\tau^{1/2})]$. Additionally, flow velocities based on LSCI represented as $1/K^2$ and entropy parameter denoted as $1-\mathcal{H}$ are included in the comparison (see Figure 6). The results depicted in Figure 6 illustrate the flow of a 5% intralipid solution within vessels, juxtaposed against the background of microcirculations within a sponge.

It should be noted that there is an evident lack of sensitivity to blood flow in the minor vessels, as illustrated in Figure 5c. The phantom measurements (see Figure 6b) demonstrate that the configuration of the curve of the obtained parameters of flow corresponds to the linear increase in flow. This is particularly evident for the $\max[\nabla g_1(\tau^{1/2})]$ parameter, where flows below 10μl min^{-1} do not contribute to an increase in the signal. The LDF demonstrates steeper slope at slower flow rates, while LSCI excels in detecting higher flow rates (refer to Figure 6b). Notably, the DCS approach and laser speckles processed with entropy exhibit comparable curves. The variations in the values in the two representations of DCS-based results stem from the selection of different orders of correlation time (average times for the decorrelation analysis of intensity fluctuations, τ and τ^2) used in the characterization of the slope of the autocorrelation function of the backscattered light.[4]

The comparison of the utilized DLS-based approaches in terms of sensitivity to the flow is shown at Figure 6c and is based on the following definition[77]:

$$S_a = \left|\frac{d\Phi}{dv}\right| \tag{13}$$

where Φ is the DLS-based approach measured parameter (i.e. $\mathcal{J}$, $\ln[g_2(\tau_{min})-1]/\Delta\tau$, $max[\nabla g_1(\tau^{1/2})]$, $(1-\mathcal{H})$ or $1/K^2$). As one can see the $\mathcal{J}$ parameter exhibits significantly greater intensity compared to other approaches at low flow rates ($0-20$ μl min^{-1}). Conversely, the lowest sensitivity at these flow rates is observed for the $1/K^2$ parameter. For flow rates in the range of $20-40$ μl min^{-1}, the highest sensitivity is achieved by the entropy and $\max[\nabla g_1(\tau^{1/2})]$ parameters. At high flow rates ($50-100$ μl min^{-1}), the $1/K^2$ parameter becomes more sensitive compared to other parameters.

2.6. Future Perspectives

The future perspectives of DLS-based imaging modalities are centered on several key areas. Technological advancements are aimed at improving the measurement signal-to-noise ratio (SNR) and depth sensitivity through innovations such as multi-source and parallel detection systems, heterodyne/interferometric detection, multispeckle camera-based methods, long-pathlength photon selection, and operating at longer wavelengths.[4,78] Integrating these advancements is expected to result in significant improvements in SNR, enabling faster acquisition rates and

more sensitive brain perfusion measurements. Emphasis will also be placed on translating these technological advances into reliable, compact, and user-friendly instruments for clinical environments, ensuring measurement accuracy and developing robust calibration methods to make DCS data interpretable in clinically relevant units. Additionally, there is a growing need to develop wearable, low-cost DLS-based devices to facilitate broader dissemination and enable studies in naturalistic environments, similar to functional near-infrared spectroscopy (fNIRS). Continuous validation studies will be necessary to demonstrate that DCS perfusion values correlate with established MRI and CT perfusion quantification methods, and establishing normative ranges will be critical for clinical adoption. Movement artifacts are significant issues that limit the clinical application of all DLS-based modalities. Any movement of the observed object leads to changes in the measured speckle intensity value, making the development of motion artifact correction approaches crucial for speckle contrast imaging. Several studies have already proposed methods for correcting motion artifacts in LSCI, including both software[31,79,80] and hardware[81,82] solutions. By addressing these areas, DCS has the potential to become a widely used tool for clinical decision-making and functional imaging studies, advancing the noninvasive monitoring of deep tissue perfusion.

Another promising paths for future improvement of DLS-based blood flow imaging technology is the development of multi-modal approaches that combine DCS with other imaging and/or electrophysiological modalities, such as optical coherence tomography (OCT) and fluorescent intravital microscopy (FIM).[4] Multi-modal assessment holds significant promise for clinical use as it enables the monitoring of multiple parameters in biological processes. Additionally, the integration of artificial intelligence (AI), machine learning (ML), and deep-learning (DL) algorithms offers a transformative potential for enhancing DLS-based imaging[83] These technologies can improve the accuracy and efficiency of image analysis, facilitate real-time processing, and develop advanced motion artifact correction techniques, further expanding the clinical applicability of DLS.

To ensure the clinical utility and widespread adoption of DCS, future efforts should focus on translating technological advances into reliable, compact, and user-friendly instruments tailored for clinical environments. This involves ensuring measurement accuracy and developing robust calibration methods to render DCS data interpretable in clinically relevant units. Additionally, there is a pressing need to develop wearable, low-cost DCS devices to broaden the technology's dissemination and enable studies in naturalistic environments.[84] Furthermore, continuous validation studies are essential to demonstrate that DCS perfusion values correlate with established MRI and CT perfusion quantification methods, establishing normative ranges to guarantee the accuracy of absolute perfusion values for clinical adoption.

Finally, we anticipate that the integration of Orbital Angular Momentum (OAM) of light[85] in DCS can significantly enhance the resolution and accuracy of blood flow measurements. The mechanism behind this improvement involves the unique properties of OAM light, which can encode information in the OAM phase of the light wave. This phase information, when preserved as OAM phase memory,[86] allows for deeper and more precise tracking of scattered photons, thus enabling more accurate measurements of the velocity and direction of blood flow. Although integrating OAM into DCS and/or LSCI is still an emerging research area, continued advancements in DLS-based imaging technologies will pave the way for groundbreaking developments and new insights into blood flow diagnostic imaging. In clinical settings, enhanced resolution and accuracy are crucial for the detailed characterization of microvascular blood flow, which is essential for diagnosing and monitoring various medical conditions. The ability to detect subtle changes in blood flow direction and velocity can lead to a better understanding and treatment of diseases that affect blood circulation.

3. Summary and Conclusion

In the current study, we evaluated various DLS-based imaging modalities and their application in transcranial blood flow imaging, emphasizing quantitative processing enhancements. Employing an advanced experimental setup featuring a high-speed camera and NIR laser, we achieved robust transcranial blood flow visualization, demonstrating the DLS-based setup's capability to provide high-quality imaging while minimizing potential tissue damage. This setup's effectiveness was further validated using a sophisticated optical small animal phantom, confirming the system's accuracy in cerebral blood flow reconstruction. Our in vivo experiments on anesthetized mice, incorporating SNP to modulate cerebral blood flow, demonstrated our system's sensitivity to dynamic changes in blood perfusion. Through detailed analysis using autocorrelation function techniques, LSCI, and the novel introduction of entropy as a blood flow metric, we offered a nuanced understanding of cerebral hemodynamics. These methodologies allowed for the detection and visualization of subtle cerebral circulation alterations induced by SNP, highlighting the diverse applicability and robustness of DLS techniques. Moreover, spectral analysis and PCA provided deep insights into the oscillatory components of cerebral blood flow, revealing physiological mechanisms regulating blood flow and identifying areas most affected by pharmacological interventions. These advanced processing techniques underscored the complexity of cerebral microcirculation and showcased the potential for DLS-based methodologies to advance neuroscience research and clinical diagnosis. An integration of the LSCI technologies with the sophisticated image processing approaches has opened new avenues for understanding the intricacies of cerebral blood flow dynamics. By enhancing the quantitative processing of transcranial imaging, this work not only advances the field of biomedical engineering but also lays the groundwork for developing clinical strategies to address neurological conditions characterized by compromised cerebral blood flow.

The introduction of entropy as a metric for blood flow visualization marked a novel approach in this field. By focusing on the variability and unpredictability in the speckle pattern, entropy-based imaging offered a unique perspective on blood flow dynamics. This method's ability to quantify the temporal and spatial complexity of laser speckle patterns provided an alternative yet effective means of assessing blood flow in vivo.

Additionally, spectral analysis via wavelet transform has deepened understanding by analyzing oscillation amplitudes in blood perfusion, revealing physiological mechanisms during SNP infusion and emphasizing the complexity of cerebral microcirculation.

Moreover, PCA has effectively tackled noise reduction and data compression in transcranial imaging, focusing on principal components to enhance image clarity and manage large datasets. This method helps extract clinically relevant information, offering a standardized approach for transcranial data analysis.

To sum up, while DCS/DWS and LDF may seem identical, the main distinctions between them are in their technical aspects and sensitivity. In LDF, the detection method typically involves continuous-wave laser light that is scattered by moving particles (e.g., red blood cells (RBC) in blood flow). The scattered light is detected by a photodetector, which produces an electrical signal proportional to the intensity of the scattered light. The output from the photodetector is an analog signal that varies in amplitude depending on the Doppler shifts caused by the motion of the particles. This analog signal is then processed to extract information about the velocity and flow characteristics of the particles. In LSCI, the approach involves illuminating a tissue with coherent laser light and capturing the resulting speckle pattern using a camera. The speckle pattern results from the interference of scattered light waves from moving particles. The contrast of the speckle pattern (i.e., the variation in intensity) is analyzed to infer the velocity and distribution of blood flow. In LSCI, the contrast in the speckle pattern is quantified over time or across multiple frames, and this contrast is inversely related to the velocity of the scattering particles. The speckle contrast is then processed to generate maps of blood flow velocity and dynamics. LSCI provides spatially resolved, wide-field images of blood flow over large tissue areas, making it quite convenient for applications where spatial resolution and coverage are critical. In DCS/DWS, the detection method often involves single-photon counting, where highly sensitive photodetectors (such as avalanche photodiodes or Photomultiplier Tubes (PMTs)) detect individual photons scattered by particles. The distribution of photon arrival times is analyzed to determine the dynamics of the scattering particles. This method is highly sensitive and can provide detailed information about the motion of particles, especially in media where scattering is very strong. Single photon counting is generally more sensitive than analogous detection in LDF, as it can detect very low levels of scattered light and provides information at the single-photon level. LSCI, in contrast, offers high spatial resolution over a wide area but is less sensitive to deep tissue dynamics compared to DCS/DWS. Entropy analysis is a versatile statistical tool that measures the complexity or disorder in a system, applicable across a broad range of data types to reveal underlying flow patterns. Entropy is calculated based on the probability distribution of speckle intensity values. Higher entropy indicates greater complexity or randomness, while lower entropy suggests more ordered or predictable patterns. Entropy analysis of speckle patterns helps differentiate between normal and disrupted states by identifying changes in the regularity or complexity of flow dynamics. While DCS/DWS offers depth-specific information about RBC motion, entropy provides a broader view of system complexity, useful in various diagnostic and analytical contexts. PCA, by contrast, is a method for dimensionality reduction, focusing on identifying and extracting the most significant patterns in the data. While entropy offers insights into the overall complexity, PCA provides a detailed view of the underlying structure, making them complementary techniques in data analysis and interpretation.

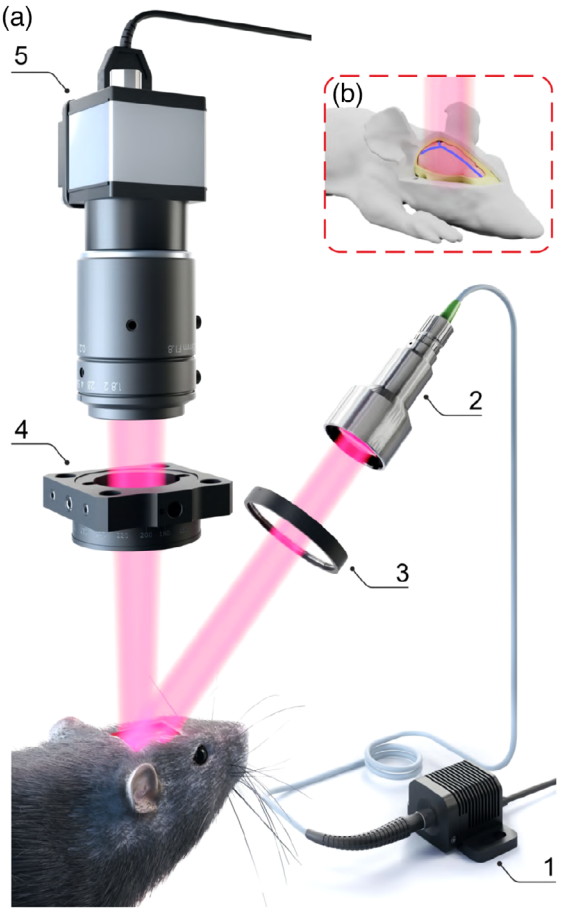

Figure 7. a) Simplified schematic presentation of high-speed full-field experimental imaging setup for transcranial blood flow visualization in-vivo, including 1 – single mode laser; 2 – collimator; 3 – linear polarizer; 4 – crossed linear polarizer; 5 – high-speed camera up to 180 000 fps. b) Mouse head phantom employed for measurement verification.

The integration of the DLS-based imaging techniques, and advanced data analysis offers an in-depth insight into the blood flow dynamics within the upper cortical layers of small laboratory animals.

The findings from this research underscore the potential of DLS-based imaging in contributing to both basic neuroscience research and the development of clinical diagnostic tools, reinforcing the significance of translating dynamic light scattering into practical applications for transcranial blood flow visualization.

4. Experimental Section

DLS-Based Experimental Imaging System: The principal scheme of optical setup used in the current study for transcranial mapping blood flow imaging is presented at **Figure 7**. The laser beam from single mode NIR 850 *nm* laser diode (QPhotonics, LLC, USA) was first collimated using a beam collimator (Thorlabs, USA). After the collimator, the power of the laser was kept at the level of 20 $mWcm^{-2}$. Further, a ground glass diffuser was used to broaden the beam (Thorlabs, USA). After, the beam illuminated the area of interest and reflected speckle pattern was registered us-

ing high-speed camera (EoSens 3CL, Germany) in combination with 50 mm objective (Kowa Optimed Deutschland GmbH, Germany) and frame grabber card (Silicon Software, Germany). To eliminate the patch of reflected light, crossed polarizers (Thorlabs, USA) were placed on the illuminating collimator and objective of the camera. This system allows for reconstruction of the blood flow image with a resolution of 150 by 100 pixels, including calculation of the temporal intensity auto-correlation function of light within the range 10^{-4} up to 1 *s*, as presented in Figure 4d. In the current study, for each experiment 96000 speckle frames were captured with a frame rate of 8000 *fps* for further processing. Obtained stack of frames was further processed in offline regime using custom-developed software in MATLAB R2022a environment. Particularly, in each pixel of stack the blood perfusion index, the steepest slope of temporal intensity autocorrelation, the maximum slope of temporal field autocorrelation, entropy and speckle contrast parameters were calculated from speckle intensity fluctuations.

Phantoms of Small Animals: For characterizing the cerebral blood flow in vivo, the developed experimental setup was tested and verified using phantom measurements before being applied to live subjects. The blood flow measurements were validated in the optical phantom of a mouse head of realistic size, shape and optical properties (Figure 6a,b). In addition to the statically scattering layer, a sponge was added inside the brain phantom that could be filled with a solution dynamically scattering light. A more accurate reproduction of the optical signals registered in the phantom was achieved by combining the model of Brownian motion of the RBC with the model of blood flow through the blood vessel. During the recordings, intralipid diluted to a concentration of 5% was driven through the embedded capillary of the phantom by the infusion pump, with different flow rates in the range of 0 – 100 µl min^{-1}. The range of flow rates was selected to embrace the typical physiological values of blood flow for the mouse brain.[87]

In-Vivo Small Animal Studies: For the in vivo measurements, 2-3 month-old C57/Bl6N mice were used. At that age, the typical thickness of the skull varies in the range of 140–150 µm.[62,88] In previous work, it was shown that these thicknesses allow for transcranial imaging without systematic errors related to the issue of non-ergodicity of the observed media.[60] The mice were anesthetized with a subcutaneous injection of ketamine (75 $mg \cdot kg^{-1}$ or 100 $mg \cdot kg^{-1}$) and xylazine (10 $mg \cdot kg^{-1}$) (KX). A thin polyethylene tube was inserted into the femoral vein and artery for the administration of nitric oxide donor sodium nitroprusside (5 $\mu g \cdot kg^{-1} min^{-1}$) and blood pressure (BP) measurements. The BP tube was connected to an in-line pressure sensors (BP-102). Data were collected with an iworx®IX-RA-834 (Iworx Systems Inc.) data acquisition system and Labscribe 4 software. The head was fixed on a head stabilizer and the scalp removed to expose the skull. All experimental procedures and animal care were in accordance with the Finnish and European legislation and were approved by the Finnish National Project Authorization Board (license numbers ESAVI/41363/2019 and ESAVI/2362/04.10.07/2017). Special care was taken during the preparation phase, where the skin overlying the skull was meticulously peeled away. It was important that the skull and its underlying structures remained intact and undamaged. This preparatory step was crucial for gaining unobstructed access to the skull, optimizing it for the novel imaging technique. To achieve a reproducible alternation in cerebral blood flow, which is essential for the reliability of our observations, we adopted a protocol involving the infusion of sodium nitroprusside (SNP) intravenously.

Acknowledgements

This study is based upon work from COST Action CA21159 - Understanding interaction light - biological surfaces: the possibility for new electronic materials and devices (PhoBioS), supported by COST (European Cooperation in Science and Technology). This study was also supported by the European Union's Horizon 2020 research and innovation programme under grant agreement No.863214 – NEUROPA project, and the Russian Science Foundation – project No. 22-65-00096.

Conflict of Interest

The authors declare no conflict of interest.

Data Availability Statement

The data that support the findings of this study are available from the corresponding author upon reasonable request.

Keywords

anscranial visualization, blood flow, diffuse correlation spectroscopy (DCS), entropy, laser doppler flowmetry (LDF), laser speckle contrast imaging (LSCI), PCA, tr hemodynamics

Received: July 2, 2023
Revised: August 20, 2024
Published online: September 20, 2024

[1] S. Fantini, A. Sassaroli, K. T. Tgavalekos, J. Kornbluth, *Neurophotonics* **2016**, *3*, 031411.
[2] L. M. Richards, S. M. S. Kazmi, K. E. Olin, J. S. Waldron, D. J. Fox Jr, A. K. Dunn, *J. Cereb. Blood Flow Metab.* **2017**, *37*, 3097.
[3] A. Konovalov, V. Gadzhiagaev, F. Grebenev, D. Stavtsev, G. Piavchenko, A. Gerasimenko, D. Telyshev, I. Meglinski, S. Eliava, *World Neurosurg.* **2023**, *171*, 35.
[4] A. Sdobnov, G. Piavchenko, A. Bykov, I. Meglinski, *Laser Photonics Rev.* **2024**, *18*, 2300494.
[5] B. Crosignani, *Statistical properties of scattered light*, Elsevier, London, **1975**.
[6] B. Berne, R. Pecora, *Dynamic Light Scattering: With Applications to Chemistry, Biology, and Physics*, Dover Books on Physics Series. Dover Publications, **2000**.
[7] D. P. Chowdhury, C. M. Sorensen, T. W. Taylor, J. F. Merklin, T. W. Lester, *Appl. Opt.* **1984**, *23*, 4149.
[8] A. B. Leung, K. I. Suh, R. R. Ansari, *Appl. Opt.* **2006**, *45*, 2186.
[9] A. P. Shepherd, P. Å. Öberg, *Laser-Doppler blood flowmetry*, vol. *107*, Springer Science & Business Media, Berlin, **2013**.
[10] E. Zherebtsov, I. Kozlov, V. Dremin, A. Bykov, A. Dunaev, I. Meglinski, *IEEE Trans. Biomed. Eng.* **2023**, *70*, 3.
[11] G. Maret, P. Wolf, *Z. Phys. B: Condens. Matter* **1987**, *65*, 409.
[12] D. Pine, D. Weitz, P. Chaikin, E. Herbolzheimer, *Phys. Rev. Lett.* **1988**, *60*, 1134.
[13] A. Fercher, J. Briers, *Opt. Commun.* **1981**, *37*, 326.
[14] R. Bandyopadhyay, A. Gittings, S. Suh, P. Dixon, D. Durian, *Rev. Sci. Instr.* **2005**, *76*, 093110.
[15] T. Durduran, R. Choe, W. B. Baker, A. G. Yodh, *Rep. Prog. Phys.* **2010**, *73*, 076701.
[16] M. M. Wu, K. Perdue, S.-T. Chan, K. A. Stephens, B. Deng, M. A. Franceschini, S. A. Carp, *Biomed. Opt. Express* **2022**, *13*, 1131.
[17] S. A. Carp, M. B. Robinson, M. A. Franceschini, *Neurophotonics* **2023**, *10*, 013509.
[18] E. J. Sie, H. Chen, E.-F. Saung, R. Catoen, T. Tiecke, M. A. Chevillet, F. Marsili, *Neurophotonics* **2020**, *7*, 035010.
[19] T. Durduran, A. G. Yodh, *NeuroImage* **2014**, *85*, 51.
[20] R. Bandyopadhyay, A. S. Gittings, S. S. Suh, P. K. Dixon, D. J. Durian, *Rev. Sci. Inst.* **2005**, *76*, 93110.

[21] C. P. Valdes, H. M. Varma, A. K. Kristoffersen, T. Dragojevic, J. P. Culver, T. Durduran, *Biomed. Opt. Express* **2014**, *5*, 2769.
[22] R. Bi, J. Dong, K. Lee, *Opt. Lett.* **2013**, *38*, 1401.
[23] J. Xu, A. K. Jahromi, J. Brake, J. E. Robinson, C. Yang, *APL Photon.* **2020**, *5*, 126102.
[24] V. Kalchenko, N. Madar-Balakirski, I. Meglinski, A. Harmelin, *J. Biophoton.* **2011**, *4*, 645.
[25] H. Ayaz, W. B. Baker, G. Blaney, D. A. Boas, H. Bortfeld, K. Brady, J. Brake, S. Brigadoi, E. M. Buckley, S. A. Carp, R. J. Cooper, K. R. Cowdrick, J. P. Culver, I. Dan, H. Dehghani, A. Devor, T. Durduran, A. T. Eggebrecht, L. L. Emberson, Q. Fang, S. Fantini, M. A. Franceschini, J. B. Fischer, J. Gervain, J. Hirsch, K.-S. Hong, R. Horstmeyer, J. M. Kainerstorfer, T. S. Ko, D. J. Licht, et al., *Neurophotonics* **2022**, *9*, S24001.
[26] D. R. Miller, R. Ashour, C. T. Sullender, A. K. Dunn, *Neurophotonics* **2022**, *9*, 021908.
[27] S. Tao, T. Zhang, K. Zhou, X. Liu, Y. Feng, W. Zhao, J. Chen, *Front. Surg.* **2022**, *9*.
[28] V. Kalchenko, K. Ziv, Y. Addadi, N. Madar-Balakirski, I. Meglinski, M. Neeman, A. Harmelin, *Laser Phys. Lett.* **2010**, *7*, 603.
[29] V. Kalchenko, D. Israeli, Y. Kuznetsov, I. Meglinski, A. Harmelin, *J. Biophoton.* **2015**, *8*, 897.
[30] V. Kalchenko, A. Sdobnov, I. Meglinski, Y. Kuznetsov, G. Molodij, A. Harmelin, *Photonics* **2019**, *6*, 80.
[31] G. Molodij, A. Sdobnov, Y. Kuznetsov, A. Harmelin, I. Meglinski, V. Kalchenko, *Phys. Med. Biol.* **2020**, *65*, 075007.
[32] I. Meglinski, A. Korolevich, V. Tuchin, *Crit. Rev. Biomed. Eng.* **2001**, *29*, 535.
[33] I. Meglinski, V. Kal'chenko, Y. Kuznetsov, B. Kuznik, V. Tuchin, *Dokl. Phys.* **2013**, *58*, 323.
[34] G. Piavchenko, I. Kozlov, V. Dremin, D. Stavtsev, E. Seryogina, K. Kandurova, V. Shupletsov, K. Lapin, A. Alekseyev, S. Kuznetsov, A. Bykov, A. Dunaev, I. Meglinski, *J. Biophoton.* **2021**, *14*, e202100216.
[35] J. He, H. Lu, L. Young, R. Deng, D. Callow, S. Tong, X. Jia, *J. Cereb. Blood Flow Metab.* **2019**, *39*, 1161.
[36] A. Sdobnov, V. Tsytsarev, G. Piavchenko, A. Bykov, I. Meglinski, *J. Biophoton.* **2024**, *10*, e202400017.
[37] L. Yin, T. Yu, L. Cheng, X. Liu, W. Zhang, H. Zhang, L. Du, W. He, *BMC Neurosci.* **2022**, *23*, 1.
[38] P. Hu, B. Niu, H. Yang, Y. Xia, D. Chen, C. Meng, K. Chen, B. Biswal, *Microcirculation* **2022**, *29*, e12783.
[39] V. Rajan, B. Varghese, T. van Leeuwen, W. Steenbergen, *Lasers Med. Sci.* **2009**, *24*, 645.
[40] B. A. Sutherland, T. Rabie, A. M. Buchan, *Laser Doppler Flowmetry to Measure Changes in Cerebral Blood Flow*, Springer New York, New York, NY, **2014**, pp. 237–248.
[41] E. Zharkikh, V. Dremin, E. Zherebtsov, A. Dunaev, I. Meglinski, *J. Biophotonics* **2020**, *13*, 202000203.
[42] K. E. Y. Claes, H. Hoeksema, T. Vyncke, J. Verbelen, P. De Coninck, I. De Decker, S. Monstrey, *J. Burn Care Res.* **2021**, *42*, 513.
[43] M. Chen, D. Wen, S. Huang, S. Gui, Z. Zhang, J. Lu, P. Li, *Opt. Lett.* **2018**, *43*, 5627.
[44] S. Uchida, F. Kagitani, *J. Physiol. Sci.* **2018**, *68*, 415.
[45] C. Crouzet, R. H. Wilson, A. Bazrafkan, M. H. Farahabadi, D. Lee, J. Alcocer, B. J. Tromberg, B. Choi, Y. Akbari, *Biomed. Opt. Express* **2016**, *7*, 4660.
[46] R. H. Wilson, C. Crouzet, M. Torabzadeh, A. K. Bazrafkan, M. Hosseini-Farahabadi, B. Jamasian, D. Donga, J. Alcocer, S. M. Zaher, B. Choi, et al., *Neurophotonics* **2017**, *4*, 045008.
[47] R. Wilson, C. Crouzet, M. Torabzadeh, A. Bazrafkan, *Neurophotonics* **2021**, *8*, 025001.
[48] Y. Zhao, K. Wang, W. Li, H. Zhang, Z. Qian, Y. Liu, *J. Biomed. Opt.* **2020**, *25*, 056005.
[49] B. Liu, S. Shah, G. Küreli, A. Devor, D. A. Boas, X. Cheng, *Biomed. Opt. Express* **2023**, *14*, 4790.
[50] K. S. Schwartz, E. N. Theis, K. Bunting, R. A. McCaughey, J. A. Lang, *Microvasc. Res.* **2022**, *142*, 104363.
[51] G. J. Hodges, P. Klentrou, S. S. Cheung, B. Falk, *Microvasc. Res.* **2020**, *128*, 103927.
[52] G. Guven, A. Dijkstra, T. M. Kuijper, N. Trommel, M. E. van Baar, A. Topeli, C. Ince, C. H. van der Vlies, *Microcirculation.* **2023**, *30*, e12795.
[53] A. Serov, W. Steenbergen, F. de Mul, *Opt. Lett.* **2002**, *27*, 300.
[54] A. Serov, B. Steinacher, T. Lasser, *Opt. Express* **2005**, *13*, 3681.
[55] A. Serov, T. Lasser, *Opt. Express* **2005**, *13*, 6416.
[56] T. B. Rice, E. Kwan, C. K. Hayakawa, A. J. Durkin, B. Choi, B. J. Tromberg, *Biomed. Opt. Express* **2013**, *4*, 2880.
[57] P. Zakharov, A. Völker, A. Buck, B. Weber, F. Scheffold, *Opt. Lett.* **2006**, *31*, 3465.
[58] A. B. Parthasarathy, S. M. S. Kazmi, A. K. Dunn, *Biomed. Opt. Express* **2010**, *1*, 246.
[59] A. Sdobnov, A. Bykov, G. Molodij, V. Kalchenko, T. Jarvinen, A. Popov, K. Kordas, I. Meglinski, *J. Phys. D Appl. Phys.* **2018**, *51*, 155401.
[60] A. Y. Sdobnov, V. Kalchenko, A. V. Bykov, A. P. Popov, G. Molodij, I. Meglinski, *Opt. Spectrosc.* **2020**, *128*, 778.
[61] S. Haleh, G. Hirac, P. Frederic, *J. Biomed. Opt.* **2017**, *22*, 10503.
[62] J.-H. Park, W. Sun, M. Cui, *Proc. Nat. Acad. Sci. USA* **2015**, *112*, 9236.
[63] S. Kim, E. Kim, E. Anguluan, J. G. Kim, *Chin. Opt. Lett.* **2022**, *20*, 011702.
[64] R. B. Panerai, A. Ferriera, O. Brum, *IEEE Trans. Biomed. Eng.* **1988**, *35*, 533.
[65] M. J. Leahy, F. F. de Mul, G. E. Nilsson, R. Maniewski, *Technol. Health Care* **1999**, *7*, 143.
[66] N. Golubova, E. Potapova, E. Seryogina, V. Dremin, *Biomed. Signal Process. Control* **2023**, *85*, 104969.
[67] D. Zhang, R. Li, M. Chen, T. Vu, H. Sheng, W. Yang, U. Hoffmann, J. Luo, J. Yao, *J. Biophoton.* **2021**, *14*, e202000478.
[68] E. J. Candès, X. Li, Y. Ma, J. Wright, *J. Ambul. Care Manag.* **2011**, *58*, 1.
[69] H. Cheng, Q. Luo, S. Zeng, S. Chen, J. Cen, H. Gong, *J. Biomed. Opt.* **2003**, *8*, 559.
[70] S. Zilpelwar, S. Zilpelwar, E. J. Sie, D. Postnov, A. I. Chen, B. Zimmermann, F. Marsili, D. A. Boas, D. A. Boas, X. Cheng, X. Cheng, *Biomed. Opt. Express* **2022**, *13*, 6533.
[71] Y. Li, R. Liu, Y. Wang, D. Wen, L. Meng, J. Lu, P. Li, *Opt. Express* **2016**, *24*, 8382.
[72] D. A. Boas, A. K. Dunn, *J. Biomed. Opt.* **2010**, *15*, 11109.
[73] M. Costa, A. L. Goldberger, C.-K. Peng, *Phys. Rev. Lett.* **2002**, *89*, 068102.
[74] J. A. Bonachela, H. Hinrichsen, M. A. Muñoz, *J. Phys. A: Math. Theor.* **2008**, *41*, 202001.
[75] O. Sieryi, A. Popov, V. Kalchenko, A. Bykov, I. Meglinski, *Proc. SPIE* **2020**, *11363*, 1136312.
[76] O. Sieryi, et al., *UK patent* **2023**, 2310784.0.
[77] S. Yuan, A. Devor, D. A. Boas, A. K. Dunn, *Appl. Opt.* **2005**, *44*, 1823.
[78] S. Carp, M. Robinson, M. Franceschini, *Neurophotonics.* **2022**, *10*, 013509.
[79] K. Venugopal, S. N. Unni, A. Bach, C. Conzen, U. Lindauer, *J. Biophoton.* **2019**, *12*, e201800408.
[80] J. Guilbert, M. Desjardins, *J. Biophoton.* **2022**, *15*, e202100218.
[81] B. Lertsakdadet, C. Dunn, A. Bahani, C. Crouzet, B. Choi, *Biomed. Opt. Express* **2019**, *10*, 5149.
[82] B. Lertsakdadet, B. Y. Yang, C. E. Dunn, A. Ponticorvo, C. Crouzet, N. Bernal, A. J. Durkin, B. Choi, *J. Biomed. Opt.* **2018**, *23*, 36006.

[83] K. W. Walek, S. Stefan, J.-H. Lee, P. Puttigampala, A. H. Kim, S. W. Park, P. J. Marchand, F. Lesage, T. Liu, Y.-W. A. Huang, et al., *Nat. Commun.* **2023**, *14*, 2982.
[84] E. James, P. R. T. Munro, *Sensors* **2023**, *23*, 23.
[85] A. M. Yao, M. J. Padgett, *Adv. Opt. Photon.* **2011**, *3*, 161.
[86] I. Meglinski, I. Lopushenko, A. Sdobnov, A. Bykov, *Light Sci. Appl.* **2024**.
[87] C. Hall, E. Lueshen, A. Mošat', A. A. Linninger, *J. Pharm. Sci.* **2012**, *101*, 1221.
[88] D. Li, Z. Zheng, T. Yu, B. Tang, P. Fei, J. Qian, Z. Dan, *J. Biophoton.* **2020**, e202000142.